A Study of Deterministic Jitter in Crystal Oscillators

Paolo Maffezzoni, *Member, IEEE*, Zheng Zhang, *Student Member, IEEE*, and Luca Daniel, *Member, IEEE*

Abstract—**Crystal oscillators are widely used in electronic systems to provide reference timing signals. Even though they are designed to be highly stable, their performance can be deteriorated by several types of random noise sources and deterministic interferences. This paper investigates the phenomenon of timing jitter in crystal oscillators induced by the injection of deterministic interferences. It is shown that timing jitter is closely related to the phase and amplitude modulations of the oscillator response. A closed-form variational macromodel is proposed to quantify timing jitter as well as to qualitatively explain the interference mechanism. Analytical results and efficient numerical simulations are developed to explore how timing jitter depends on the frequency of the interfering signal. The methodology is tested by a crystal Pierce oscillator.**

Index Terms—**Amplitude and phase modulation, crystal oscillators, oscillator macromodeling, system reliability, timing jitter.**

I. INTRODUCTION

CRYSTAL oscillators are currently employed in a huge number of electronic applications including consumer and industrial electronics, research and metrology as well as military and aerospace [1]. As fundamental blocks of many communication systems, crystal oscillators can provide timing signals for channel selection and frequency translation. In digital electronics, they are widely employed to generate synchronization clock signals.

Even though crystal oscillators are designed to be highly stable, the accuracy of their response can be deteriorated by random noise sources and deterministic interferences. The latter, in particular, refer to "well defined signals" which are caused by unwanted effects such as electromagnetic interferences (EMI), crosstalk or power supply line fluctuations [2], [3]. In today's high-frequency integrated circuits, deterministic interferences have become a major concern. The deterioration of the oscillator response due to deterministic signals is commonly described by *timing jitter*, i.e., the deviation of the actual output waveform from the ideal one at time axis.

Predicting the timing jitter induced by potential deterministic interferences, i.e., *deterministic jitter*, is a difficult issue.

Deterministic jitter is, in fact, the result of a complex interference mechanism that involves both phase-modulation (PM) and amplitude-modulation (AM) of the oscillator response. Furthermore, the response susceptibility to interferences may change dramatically depending on the injection point and the frequency of the interfering signal. Exploring such a multifaceted behavior via repeated transistor-level CAD simulations is too time consuming, especially because of the high-Q of crystal oscillators [4], [5]. In fact, high-Q oscillators exhibit very long transient responses before reaching the steady-states.

Unfortunately, such repeated simulations normally give little insight about the complex interference mechanisms. A much more effective approach is to build a proper macromodel to describe the oscillator response. In the last two decades, extensive techniques for oscillators macromodeling have been investigated since the seminal paper of Kaertner [6].

The key feature of such an approach is the introduction of a "phase variable" which allows separating the effects of PM from those due to AM. In [6], a compact equation (i.e., a scalar differential equation) for the phase variable was derived. Due to its simplicity, this phase macromodel has been adopted by many authors to study oscillator phase noise [7]–[9], as well as to investigate the complex phase-synchronization effects [10]–[16]. However, in [6] no compact equation was provided for the amplitude variable. Instead, the amplitude variable was described by a convolution integral, which is difficult to use in practice. To address this issue, in this paper, we first complete the mathematical derivation in [6] to find simplified compact equations for the amplitude variable. We show how the proposed macromodel can be solved analytically to find the phase and amplitude responses to harmonic interferences as well as to derive the associated deterministic jitter in closed form. The proposed analytical solution highlights the macromodel parameters that mainly affect deterministic jitter mechanism. It also shows the key role played by amplitude modulation effects.

As a second contribution, we show how the macromodel can be employed in behavioral simulations to efficiently calculate the deterministic jitter caused by the interfering signal. The proposed methodology can be applied to any crystal oscillator. Simulations and numerical results are presented for a Pierce crystal oscillator.

The remainder of this paper is organized as follows: in Section II, we illustrate the timing jitter mechanism as a result of PM and AM effects. In Section III, we derive a compact equation that governs the amplitude variable. Such a macromodel is used in Section IV to find the closed-form expressions for the phase and amplitude responses and for the related timing jitter. In Section V, the proposed jitter analysis is applied to a Pierce crystal oscillator, and some numerical simulation results are provided to verify the efficiency and accuracy of our

P. Maffezzoni is with the Dipartimento di Elettronica e Informazione, Politecnico di Milano, I20133, Milan, Italy (e-mail:pmaffezz@elet.polimi.it).

Z. Zhang and L. Daniel are with the Department of Electrical Engineering and Computer Science, Massachusetts Institute of Technology, Cambridge, MA 02139 USA (e-mail: z_zhang,luca@mit.edu).

Color versions of one or more of the figures in this paper are available online at http://ieeexplore.ieee.org.

proposed approach. The fundamentals of Floquet theory and computational details are reviewed in the Appendix.

II. OSCILLATOR MACROMODEL AND TIMING JITTER

The ideal noiseless crystal oscillator can be described by a set of ordinary differential equations (ODE):

$$\dot{\mathbf{x}}(t) = \mathbf{f}(\mathbf{x}(t)) \tag{1}$$

where $\mathbf{x}(t), \dot{\mathbf{x}}(t) \in \mathbf{R}^N$ are the vector of circuit variables and their time derivative respectively, $\mathbf{f} : \mathbf{R}^N \rightarrow \mathbf{R}^N$ is a vector-valued nonlinear function and t is time. A well designed crystal oscillator admits a stable T_0-periodic steady-state response $\mathbf{x}_s(t) \in \mathbf{R}^N$ (frequency $f_0 = 1/T_0$) which corresponds to a limit cycle in the phase space. The limit cycle $\mathbf{x}_s(t)$ represents the *ideal* response, i.e the oscillator response in absence of any noise and interferences. When a small-amplitude interfering signal $s_{in}(t)$ is injected into the oscillator, its equation is modified to

$$\dot{\mathbf{x}}(t) = \mathbf{f}(\mathbf{x}(t)) + \mathbf{b}(\mathbf{x}(t)) \, s_{in}(t), \tag{2}$$

where $\mathbf{b}(\cdot)$ (which depends on variables $\mathbf{x}(t)$) is the vector that inserts signal $s_{in}(t)$ into circuit equations.

According to [6], the solution $\mathbf{x}_p(t)$ to the perturbed (2) can be split in the two terms

$$\mathbf{x}_p(t) = \mathbf{x}_s(t + \alpha(t)) + \Delta\mathbf{x}(t + \alpha(t)), \tag{3}$$

where the variable $\alpha(t)$ is a time shift to the unperturbed response $\mathbf{x}_s(t)$. The first term in (3) accounts for the response variation tangent to the limit cycle (i.e., the tangential component) and thus is related to PM. The second variable $\Delta\mathbf{x}(t)$ provides the variation component transversal to the orbit (i.e., transversal component) and thus is related to AM.

Timing jitter is evaluated by considering one element of the state vector (3), i.e., $x_p^o(t) \in \mathbf{x}_p(t)$, as the *output variable* of the oscillator. For the output variable, (3) reduces to

$$x_p^o(t) = x_s^o(t + \alpha(t)) + \Delta x^o(t + \alpha(t)), \tag{4}$$

where $x_s^o(\cdot) \in \mathbf{x}_s(\cdot)$ and $\Delta x^o(\cdot) \in \Delta\mathbf{x}(\cdot)$ are the corresponding vector elements.

We are interested in the time points t_k where the output variable waveform $x_p^o(t)$ crosses a given threshold X_{th} with a positive slope, as depicted in Fig. 1. Two consecutive crossing times t_k and t_{k+1} define the value of the perturbed period $T_k = t_{k+1} - t_k$ over the kth cycle. In the presence of an interference, T_k will differ from the ideal value T_0. The standard deviation of the period values T_k gives the timing jitter σ_T.

We analyze first the case where AM effects are negligible, i.e., in (4) $\Delta x^o(t + \alpha(t)) = 0$, and thus the perturbed response is a purely time-shifted version of the ideal one, as portrayed in Fig. 1 (top). In this case, crossing time points t_k and t_{k+1} are decided (along with the condition on the slope sign) according to

$$x_s^o(t_k + \alpha(t_k)) = x_s^o(t_{k+1} + \alpha(t_{k+1})) = X_{th} \tag{5}$$
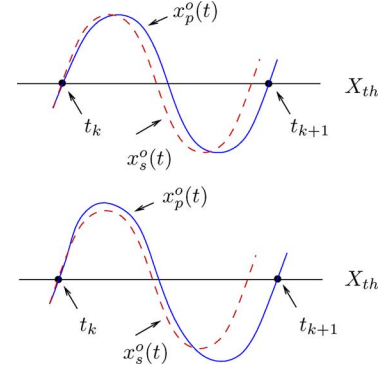

Fig. 1. Timing jitter measures the variations of the crossing times of the perturbed response $x_p^o(t)$ with respect to those of the ideal response $x_s^o(t)$. Top: with PM effect only; bottom: with both PM and AM effects.

and thus, due to the T_0-periodicity of waveform $x_s^o(\cdot)$, they satisfy the following relation

$$t_{k+1} + \alpha(t_{k+1}) = t_k + \alpha(t_k) + T_0. \tag{6}$$

During the k-th cycle, the period of the perturbed response is

$$T_k = t_{k+1} - t_k = \alpha(t_k) - \alpha(t_{k+1}) + T_0. \tag{7}$$

As we will see in Section IV, in the presence of an harmonic interference, the waveform $\alpha(t)$ oscillates with (angular) frequency $\Omega_m \ll \omega_0$ and thus, in view of (7), the fluctuations of the perturbed period are well approximated by

$$T_k - T_0 \approx -\dot{\alpha}(t_k)T_0. \tag{8}$$

We proceed to consider the case where both PM and AM effects are significant, as shown in Fig. 1 (bottom). In this case, relation (5) is modified to

$$x_s^o(t_k + \alpha(t_k)) + \Delta x^0(t_k + \alpha(t_k))$$
$$= X_{th} = x_s^o(t_{k+1} + \alpha(t_{k+1})) + \Delta x^0(t_{k+1} + \alpha(t_{k+1})). \tag{9}$$

The extra jitter due to AM, denoted as δT_k, enters time relationship (6) as follows[1]

$$t_{k+1} + \alpha(t_{k+1}) = t_k + \alpha(t_k) + T_0 + \delta T_k. \tag{10}$$

Since in (10) $\delta T_k \ll T_0$, the first term on the right hand side of (9) is well approximated by

$$x_s^o(t_{k+1} + \alpha(t_{k+1}))$$
$$= x_s^o(t_k + \alpha(t_k) + T_0 + \delta T_k)$$
$$\approx x_s^o(t_k + \alpha(t_k) + T_0) + \dot{x}_s^o(t_k + \alpha(t_k) + T_0)\,\delta T_k. \tag{11}$$

The error introduced by this approximation is of the order of $(\delta T_k)^2$ and thus it is negligible compared to δT_k. Thus, plugging

[1]Note that with both PM and AM effects, the perturbed period obtained from (10) reads $T_k = t_{k+1} - t_k = \underbrace{\alpha(t_k) - \alpha(t_{k+1})}_{PM} + \underbrace{\delta T_k}_{AM} + T_0$.

(11) into (9) and exploiting the T_0-periodicity of $x_s^o(\cdot)$ and of $\dot{x}_s^o(\cdot)$, we obtain

$$\delta T_k = \frac{\Delta x^0(t_k + \alpha(t_k)) - \Delta x^0(t_{k+1} + \alpha(t_{k+1}))}{\dot{x}_s^o(t_k + \alpha(t_k))}. \quad (12)$$

In Section IV, it will be proven that, for a harmonic interference, the amplitude waveform takes the form

$$\Delta x^o(t) = u_2(t) \cdot y_2(t), \quad (13)$$

where $u_2(t)$ is a T_0-periodic function (i.e., an element of a Floquet eigenvector) while $y_2(t)$ is a slowly-varying coefficient oscillating with frequency $\Omega_m \ll \omega_0$. In this case, using the approximation $T_0 + \delta T_k \approx T_0$ and the periodicity of $u_2(t)$, the numerator of (12) can be simplified to

$$\begin{aligned} \Delta x^0&(t_k + \alpha(t_k)) - \Delta x^0(t_{k+1} + \alpha(t_{k+1})) \\ &\approx u_2(t_k + \alpha(t_k)) \cdot [y_2(t_k + \alpha(t_k)) - y_2(t_{k+1} + \alpha(t_{k+1}))] \\ &\approx - u_2(t_k + \alpha(t_k)) \cdot \dot{y}_2(t_k + \alpha(t_k)) T_0. \end{aligned} \quad (14)$$

With this simplification, AM-induced period variation (12) is estimated by

$$\delta T_k \approx -R \dot{y}(t_k + \alpha(t_k))T_0, \quad (15)$$

where $R = u_2(t_k + \alpha(t_k))/\dot{x}_s^o(t_k + \alpha(t_k))$ is the ratio of $u_2(t)$ over $\dot{x}_s(t)$ at the crossing time point t_k, which is almost constant over all cycles. From (15), we see that to minimize the AM-induced jitter the threshold value X_{th} should be selected to maximize the time slope of the ideal response $x_s(t)$ at the crossing point.

III. PHASE AND AMPLITUDE EQUATIONS

In this section, we first review the scalar ODE that governs the phase variable. After that, for the first time, we provide a similar compact model for the amplitude variable.

A. Review of Phase Model

Substituting the perturbed solution (3) into (2) and neglecting the higher-order terms in $\Delta \mathbf{x}$, $\dot{\alpha}(t)$, $s_{in}(t)$, we get

$$\dot{\mathbf{x}}_s(\tau)\dot{\alpha}(t) + \Delta \dot{\mathbf{x}}(\tau) = \text{Df}(\mathbf{x}_s(\tau)) \cdot \Delta \mathbf{x}(\tau) + \mathbf{b}(\mathbf{x}_s(\tau)) s_{in}(t), \quad (16)$$

where

$$\tau = t + \alpha(t) \quad (17)$$

is a scaled time, "·" denotes derivative with respect to variable t and

$$\text{Df}(\mathbf{x}_s(t)) = \left. \frac{\partial \mathbf{f}(\mathbf{x})}{\partial \mathbf{x}} \right|_{\mathbf{x} = \mathbf{x}_s(t)} \quad (18)$$

is the Jacobian of function $\mathbf{f}(\cdot)$ computed along the stable orbit.

Starting from (16), Kaertner in [6] proposed the following scalar equation for the phase variable

$$\dot{\alpha}(t) = \Gamma_1(t + \alpha(t)) s_{in}(t), \quad (19)$$

where

$$\Gamma_1(t) = \mathbf{v}_1^T(t) \cdot \mathbf{b}(\mathbf{x}_s(t)) \quad (20)$$

is a scalar T_0-periodic function that projects the external signal along the first left Floquet eigenvector $\mathbf{v}_1(t)$ whose definition is reviewed in Appendix A.

B. Amplitude Model

Now, we derive similar equations for the amplitude variable. We first observe that the amplitude variation in (3) can be expanded as follows

$$\Delta \mathbf{x}(t + \alpha(t)) = \sum_{j=2}^{N} \mathbf{u}_j(t + \alpha(t)) \widetilde{y}_j(t), \quad (21)$$

where $\mathbf{u}_j(t)$ is the jth right Floquet eigenvector, as described in Appendix A, and

$$\widetilde{y}_j(t) = y_j(\tau) = y_j(t + \alpha(t)) \quad (22)$$

is an *unknown scalar function* of time. To find the ODE that governs $y_k(t)$, we multiply the left-hand side of (16) by $\mathbf{v}_k^T(\tau)$ with $k > 1$. By exploiting the biorthogonality condition $\mathbf{v}_k^T(\tau) \cdot \dot{\mathbf{x}}_s(\tau) = 0$, we obtain

$$\begin{aligned} \mathbf{v}_k^T(\tau) \cdot \Delta \dot{\mathbf{x}}(\tau) = \mathbf{v}_k^T(\tau) \cdot \text{Df}(\mathbf{x}_s(\tau)) \cdot \Delta \mathbf{x}(\tau) \\ + \mathbf{v}_k^T(\tau) \cdot \mathbf{b}(\mathbf{x}_s(\tau)) s_{in}(t). \end{aligned} \quad (23)$$

According to (21) and (63), the left-hand side of (23) can be converted to

$$\mathbf{v}_k^T(\tau) \cdot \sum_{j=2}^{N} \dot{\mathbf{u}}_j(\tau) y_j(\tau) + \dot{y}_k(\tau). \quad (24)$$

Similarly, using (62), (21) and (63), the right-hand side of (23) is rewritten as

$$\lambda_k y_k(\tau) - \dot{\mathbf{v}}_k^T(\tau) \cdot \sum_{j=2}^{N} \mathbf{u}_j(\tau) y_j(\tau) + \mathbf{v}_k^T(\tau) \cdot \mathbf{b}(\mathbf{x}_s(\tau)) s_{in}(t), \quad (25)$$

where λ_k is the kth Floquet exponent described in Appendix A. Then, equating (24) to (25) and reordering we find

$$\dot{y}_k(\tau) = \lambda_k y_k(\tau) + \mathbf{v}_k^T(\tau) \cdot \mathbf{b}(\mathbf{x}_s(\tau)) s_{in}(t) - \text{Z} \quad (26)$$

where the term Z is zero, i.e.,

$$\begin{aligned} \text{Z} &= \mathbf{v}_k^T(\tau) \cdot \sum_{j=2}^{N} \dot{\mathbf{u}}_j(\tau) y_j(\tau) + \dot{\mathbf{v}}_k^T(\tau) \cdot \sum_{j=2}^{N} \mathbf{u}_j(\tau) y_j(\tau) \\ &= \sum_{j=2}^{N} \left(\mathbf{v}_k^T(\tau) \cdot \dot{\mathbf{u}}_j(\tau) + \dot{\mathbf{v}}_k^T(\tau) \cdot \mathbf{u}_j(\tau) \right) y_j(\tau) \\ &= \sum_{j=2}^{N} \frac{d}{dt} \left(\mathbf{v}_k^T(\tau) \cdot \mathbf{u}_j(\tau) \right) y_j(\tau) = \sum_{j=2}^{N} \frac{d\delta_{kj}}{dt} y_j(\tau) = 0 \quad (27) \end{aligned}$$

with δ_{kj} defined in (63). Finally, using (22), (26) can be rewritten as

$$\dot{\widetilde{y}}_k(t) = \lambda_k \, \widetilde{y}_k(t) + \Gamma_k(t + \alpha(t)) \, s_{in}(t) \qquad (28)$$

with

$$\Gamma_k(t) = \mathbf{v}_k^T(\tau) \cdot \mathbf{b}(\mathbf{x}_s(t)) \qquad (29)$$

being the scalar T_0-periodic function obtained by projecting the external signal onto the kth Floquet eigenvector $\mathbf{v}_k(t)$.

Once the Floquet eigenvalues/eigenvectors are calculated, as described in Appendix B, the response to an interfering signal $s_{in}(t)$ can be determined efficiently by two steps. First we integrate the scalar ODE (19) to obtain $\alpha(t)$; next we integrate the scalar linear ODE (28) to compute $\widetilde{y}_k(t)^2$ for $k = 2, \ldots, N$. In practice, the above mentioned procedures can be further simplified after observing (as will be shown in Section IV) that the magnitude of variables $\widetilde{y}_k(t)$ is inversely proportional to the real part (in module) of the corresponding Floquet exponent $|\text{Re}(\lambda_k)|$. Therefore, if Floquet exponents λ_k are ordered in the way that $|\text{Re}(\lambda_k)| < |\text{Re}(\lambda_{k+1})|$, only the very first functions $\widetilde{y}_k(t)$ need to be calculated. In addition, for those oscillators with highly stable limit cycles, as it is commonly the case for crystal oscillators, Floquet exponents λ_k are purely real [18] (e.g., see Table II).

IV. CRYSTAL OSCILLATORS COMPACT MACROMODEL

Further insights about deterministic jitter in crystal oscillators can be gained by considering the following macromodel

$$\begin{cases} x_p^o(t) = x_s^o(t + \alpha(t)) + \Delta x^o(t + \alpha(t)) \\ \Delta x^o(t + \alpha(t)) = u_2^o(t + \alpha(t)) \, \widetilde{y}_2(t), \end{cases} \qquad (30)$$

where $\mathbf{u}_2(t)$ and $\mathbf{v}_2(t)$ are the right and left eigenvectors corresponding to the Floquet exponent λ_2, respectively, which dominates the AM response. The phase and amplitude variables $\alpha(t)$, $\widetilde{y}_2(t)$ are found by integrating the following scalar ODEs

$$\begin{cases} \dot{\alpha}(t) = \Gamma_1(t + \alpha(t)) \, s_{in}(t) \\ \dot{\widetilde{y}}_2(t) = \lambda_2 \, \widetilde{y}_2(t) + \Gamma_2(t + \alpha(t)) \, s_{in}(t) \end{cases} \qquad (31)$$

where the projection functions $\Gamma_k(t)$, with $k = 1, 2$ are T_0-periodic and admit the Fourier expansions

$$\Gamma_k(t) = \sum_{n=0}^{\infty} \Gamma_k^n \cos(n\omega_0 t + \gamma_k^n) \qquad (32)$$

with $\gamma_k^0 = 0$.

In the remainder of this section, we will exploit this compact macromodel to evaluate analytically the phase and amplitude responses to a harmonic interference of the type

$$s_{in}(t) = A_{in} \cos(\omega_{in} t), \qquad (33)$$

where the frequency of the interference

$$\omega_{in} = m \, \omega_0 - \Delta\omega \qquad (34)$$

is expressed in terms of its detuning $|\Delta\omega| \ll \omega_0$ from the nearest mth harmonic $m\omega_0$.

A. Phase Response

Substituting (33) and (32) (with $k = 1$) in the first equation of (31), we find that the average behavior of the time derivative of $\alpha(t)$ is dominated by the slowly-varying term which arises for $n = m$

$$\dot{\alpha}(t) \approx \frac{\Gamma_1^m A_{in}}{2} \cos\left(\Delta\omega \, t + m\omega_0 \alpha(t) + \gamma_1^m\right). \qquad (35)$$

Introducing the angle

$$\theta(t) = \Delta\omega t + m\omega_0 \alpha(t) + \gamma_1^m - \frac{\pi}{2}, \qquad (36)$$

and using the notation

$$B = m\frac{\omega_0 \Gamma_1^m A_{in}}{2}, \qquad (37)$$

(35) can be rewritten as

$$\frac{d\theta(t)}{dt} = \Delta\omega - B\sin(\theta(t)) \qquad (38)$$

which is identical to the (9) b) discussed by Adler in [17] (in that reference, variable $\theta(t)$ is denoted as $\alpha(t)$). Under the condition

$$K = \frac{\Delta\omega}{B} \geq 1, \qquad (39)$$

the differential (38) admits the following closed-form solution [17]

$$\frac{\theta(t)}{2} = \text{atan}\left[\frac{1}{K} + \frac{\sqrt{K^2 - 1}}{K}\tan\left(\frac{B(t - t_0)}{2}\sqrt{K^2 - 1}\right)\right], \qquad (40)$$

and then from (36), we get

$$m\omega_0\alpha(t) = \theta(t) - \Delta\omega t - \gamma_1^m + \frac{\pi}{2}. \qquad (41)$$

The term $(B(t - t_0)/2)\sqrt{K^2 - 1}$ in (40) grows linearly with time and passes through the values $\pi/2, 3\pi/2, \ldots$ at which the tangent at the right-hand side becomes $\pm\infty$. At the same time instants $\theta(t)/2$ must also be $\pi/2, 3\pi/2, \ldots$ while it assumes values different from $(B(t - t_0)/2)\sqrt{K^2 - 1}$ during the time intervals. This means that $\theta(t)$ can be written as the superposition of a term that varies linearly with time with the average slope

$$\Omega_m = \langle\dot{\theta}(t)\rangle = B\sqrt{K^2 - 1} = \Delta\omega\sqrt{\frac{K^2 - 1}{K^2}}, \qquad (42)$$

where $\langle\cdot\rangle$ denotes the time averaging operator, and of a bounded periodic function [17]. To a first order approximation, $\theta(t)$ in (41) can be replaced with its linearly varying component $\Omega_m t$

$$m\omega_0\alpha(t) \approx \Omega_m t - \Delta\omega t, \qquad (43)$$

---

[2]In the case λ_k is complex, (28) is integrated in the complex field.

where we have imposed the initial condition $\alpha(0) = 0$. Then, substituting (43) into the right-hand-side of (35), we find

$$\dot{\alpha}(t) \approx \frac{\Gamma_1^m A_{in}}{2} \cos\left(\Omega_m t + \gamma_1^m\right). \qquad (44)$$

The PM-induced period fluctuations (8) are thus given by the samples of the following sinusoidal waveform

$$T_k - T_0 \approx -\frac{T_0\, \Gamma_1^m A_{in}}{2} \cos\left(\Omega_m t_k + \gamma_1^m\right). \qquad (45)$$

Since $\omega_0 \gg \Omega_m$, the sampling interval $\approx T_0 = 2\pi/\omega_0$ is much shorter than $2\pi/\Omega_m$. As a result, the timing jitter corresponds to the effective value of the sine wave, as follows

$$\sigma_T^{PM} = \frac{T_0 \Gamma_1^m A_{in}}{\sqrt{8}}. \qquad (46)$$

In a similar way, we can employ (43) to evaluate the frequency of the perturbed response. First, we observe that the ideal response $x_s^o(t)$ can always be written as

$$x_s^o(t) = p(\omega_0 t)$$

where $p(\cdot)$ is a generic 2π-periodic function of its argument. Next, from the first of (30) (and considering only PM effect), the perturbed output takes the form

$$x_s^o(t + \alpha(t)) = p(\omega_0 t + \omega_0 \alpha(t)) = p(\omega_p t) \qquad (47)$$

where

$$\omega_p = \omega_0 + \frac{\Omega_m - \Delta\omega}{m} \qquad (48)$$

is the perturbed angular frequency.

We conclude that for a harmonic interference of frequency ω_{in} close to $m\omega_0$, the resulting phase response and timing jitter depend on the ratio of $\Delta\omega$ over parameter B. Parameter B defined in (37), in turn, is determined by the amplitude of the interference and of the mth harmonic component of projecting function $\Gamma_1(t)$.

As an example, in Fig. 2 we plot the waveforms $m\omega_0\alpha(t)$ calculated with expression (40) for the fixed value $B = 10^4 \text{rad/s}$ and three different detunings: (i) $\Delta\omega = 1 \times B$, (ii) $\Delta\omega = 2 \times B$ and (iii) $\Delta\omega = 8 \times B$. These values lead to the three scenarios described below.

(i) Injection locking. In the limit case $K = \Delta\omega/B = 1$, from (42), we have $\theta(t) = \Omega_m = 0$ and thus from (48) we find $\omega_p = \omega_0 - \Delta\omega/m = \omega_{in}/m$. This means that the frequency of the perturbed oscillator is locked to the interference frequency divided by m. In this case, waveform $\alpha(t)$, as well as waveform $m\omega_0\alpha(t)$ shown in Fig. 2(i), varies linearly in time, implying that the period variation (45) is constant and the timing jitter σ_T^{PM} is zero. In fact, injection locking occurs also for smaller frequency detunings $\Delta\omega < B$ (please note that this case corresponds to $K < 1$ and is not covered by (40)). The critical case $\Delta\omega = B$ corresponds to the maximum detuning for which injection locking occurs which is commonly referred to as lock range [17]. We conclude that as long as the interference frequency falls within the lock range the PM-induced jitter is zero.
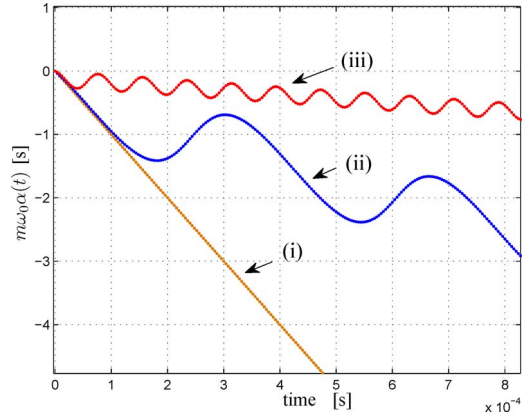

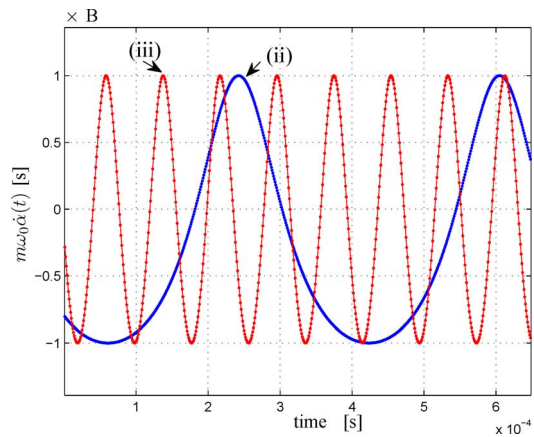Fig. 2. $m\omega_0\alpha(t)$ for the three cases (i), (ii), and (iii).

Fig. 3. $m\omega_0\dot{\alpha}(t)$ for the cases (ii) and (iii).

(ii) Strong pulling. For K slightly greater than 1, from (48) we have $0 < \Omega_m < \Delta\omega$. The mth harmonic component of the perturbed response is pulled towards the interference frequency without locking as shown in Fig. 4. In this case, waveform $m\omega_0\alpha(t)$ has a large oscillating component superimposed to the linearly varying term $(\Omega_m - \Delta\omega)\,t$, as shown in Fig. 2(ii).

(iii) Weak pulling. For $K = \Delta\omega/B \gg 1$, from (48), we find $\Omega_m \approx \Delta\omega$ and $\omega_p \approx \omega_0$, i.e., the fundamental and harmonic frequencies of the oscillator are not (significantly) affected by the interference. In this case, waveform $m\omega_0\alpha(t)$ has a small-amplitude oscillation superimposed to the linearly varying term $(\Omega_m - \Delta\omega)\,t$ as shown in Fig. 2(iii).

Furthermore, in both cases (ii) and (iii), the time derivative waveforms $m\omega_0\dot{\alpha}(t)$ plotted in Fig. 3 fluctuate between the peak values $\pm B$ as correctly predicted by (45). *We conclude that when ω_{in} falls outside the lock range, the PM-induced timing jitter σ_T^{PM} is well estimated by (46) and its value is independent of the detuning value.*

B. Amplitude Response

From the second term of (31) we know that $\widetilde{y}_2(t)$ can be considered as the output of a linear system, shown in Fig. 5, with impulse response $h(t) = \exp(\lambda_2 t)\, \text{sca}(t)$, (with $\text{sca}(\cdot)$ being the
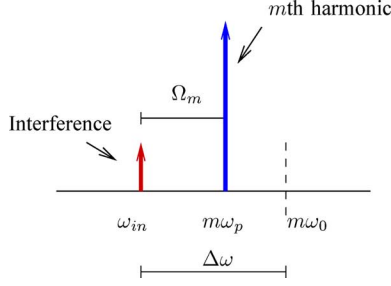
Fig. 4. Effect of PM on the output spectrum: the mth harmonic component moves from the ideal frequency $m\omega_0$ to $m\omega_p$ towards the interference frequency ω_{in}.
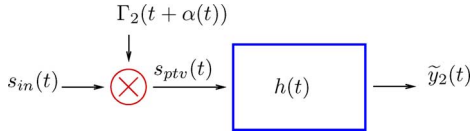

Fig. 5. Linear system for the computation of the amplitude response. The system is driven by a periodically-time-varying input $s_{ptv}(t)$ which depends on phase variable $\alpha(t)$.

ideal step function), when driven by the following periodically time-varying input

$$s_{ptv}(t) = \Gamma_2(t + \alpha(t)) \cdot s_{in}(t). \tag{49}$$

From (33) with $\omega_{in} = m\omega_0 - \Delta\omega$, (32) with $k = 2$, and (43), we obtain that this input signal $s_{ptv}(t)$ is dominated by the slowly varying harmonic

$$
\begin{aligned}
s_{ptv}(t) &\approx \frac{A_{in}\Gamma_2^m}{2} \cos(\Delta\omega t + m\omega_0\alpha(t) + \gamma_2^m) \\
&= \frac{A_{in}\Gamma_2^m}{2} \cos(\Omega_m t + \gamma_2^m). \tag{50}
\end{aligned}
$$

Hence, replacing the second term of (31) with the averaged input (50) and solving the resulting equation, we obtain

$$\widetilde{y}_2(t) = \frac{A_{in}\Gamma_2^m}{2\sqrt{\Omega_m^2 + \lambda_2^2}} \cos\left(\Omega_m t + \gamma_2^m + \operatorname{atan}\left(\frac{\Omega_m}{\lambda_2}\right)\right). \tag{51}$$

The corresponding time derivative reads

$$\dot{\widetilde{y}}_2(t) = \frac{A_{in}\Gamma_2^m}{2} M(\Omega_m) \cos\left(\Omega_m t + \gamma_2^m + \frac{\pi}{2} + \varphi(\Omega_m)\right), \tag{52}$$

with

$$
\begin{aligned}
M(\Omega_m) &= \frac{\Omega_m}{\sqrt{\Omega_m^2 + \lambda_2^2}} \\
\varphi(\Omega_m) &= \operatorname{atan}\left(\frac{\Omega_m}{\lambda_2}\right). \tag{53}
\end{aligned}
$$

The AM-induced period fluctuations δT_k are finally obtained by inserting time derivative (52) into (15), i.e.,

$$\delta T_k \approx -\frac{R\,T_0\,A_{in}\Gamma_2^m}{2} M(\Omega_m)\cos\left(\Omega_m t_k + \gamma_2^m + \frac{\pi}{2} + \varphi(\Omega_m)\right). \tag{54}$$

At this stage it is instructive to investigate the amplitude responses corresponding to the three scenarios discussed in Section IV-A. In Case (i) of injection locking, we have $\Omega_m = 0$ and thus $M(\Omega_m) = 0$, meaning that the AM-induced period fluctuation (54) is zero. In this scenario, $\widetilde{y}_2(t) = \widetilde{y}$ is constant and thus the amplitude modulation

$$\Delta x^o(t + \alpha(t)) = \widetilde{y} \cdot u_2(t + \alpha(t)) \tag{55}$$

oscillates exactly at the same frequency $\omega_p = \omega_{in}/m$ as $x_s^o(t + \alpha(t))$ in (47). The total perturbed response $x_p^o(t)$ is thus locked to ω_{in}/m with both AM-induced and PM-induced jitter being zero.[3]

By contrast, in Cases (ii) and (iii) of strong and weak pulling, respectively, the AM-induced period fluctuation (54) is non zero and should be added to the PM-induced fluctuation (45). Over each cycle, the total period variation is thus the sum of the two sine waveforms

$$
\begin{aligned}
T_k - T_0 &\approx D_1 \cos(\Omega_m t_k) \\
&\quad + D_2 M(\Omega_m) \cos(\Omega_m t_k + \Delta\gamma + \varphi(\Omega_m)) \tag{56}
\end{aligned}
$$

with $\Omega_m(\Delta\omega)$ defined in (42) and

$$
\begin{aligned}
D_1 &= T_0 \frac{\Gamma_1^m A_{in}}{2} \\
D_2 &= R\,T_0 \frac{\Gamma_2^m A_{in}}{2} \\
\Delta\gamma &= \gamma_2^m - \gamma_1^m + \frac{\pi}{2}. \tag{57}
\end{aligned}
$$

To further investigate how the total jitter depends on the interference frequency, we consider an example with realistic parameter values $D_1 = 2$ ps, $D_2 = D_1/2$, $\Delta\gamma = 0$, $B = 10^4$ rad/s, $|\lambda_2| = 10^5$ rad/s and $m = 1$ in (34). In Fig. 6 we report the total jitter, i.e., the effective value of (56), as a function of the frequency detuning $-\Delta\omega$. The magnitude of the period fluctuation due to the PM effect, i.e., first part in the right-hand side of (56), and the corresponding timing jitter are both independent of frequency detuning $\Delta\omega$. Conversely, the magnitude and the phase of the period fluctuation induced by the AM effect, i.e., the second term on the right-hand side of (56), grows with $\Delta\omega$. As a result, the total timing jitter exhibits maximum/minimal values when $(-\Delta\omega) \approx \mp|\lambda_2|$ or, equivalently, $\omega_{in} \approx \omega_0 \mp |\lambda_2|$.

V. NUMERICAL RESULTS

As an application, we study the Pierce crystal oscillator shown in Fig. 7 with the parameters collected in Table I. We adopt Spice 3 MOS models with parameter values: $V_{th_0} = 0.5$ V, $\lambda = 5 \cdot 10^{-2}$ V^{-1}, $k_n = 120$ μA/V^2, $k_p = 50$ μA/V^2. Numerical simulations are performed in

---

[3]It is worth noting here that the result in (55), whose correctness is confirmed by transistor-level simulations, is due to the form of the amplitude equation in (31). In fact, in (31) the input term (49) is weighted by the phase-modulated $\Gamma_2(t + \alpha(t))$ function. If this phase modulation were not included in the amplitude equation, the solution of this later (in the injection locking case) would give a nonconstant $\widetilde{y}_2(t)$ and a wrong nonzero AM-induced jitter.
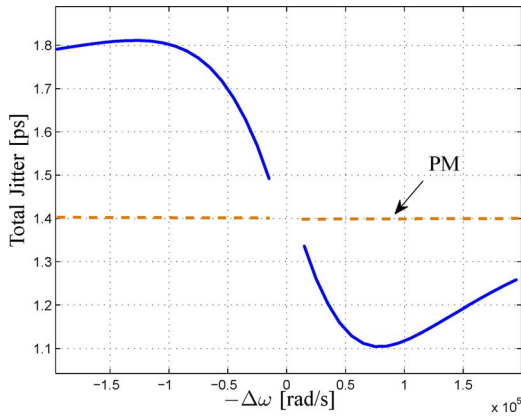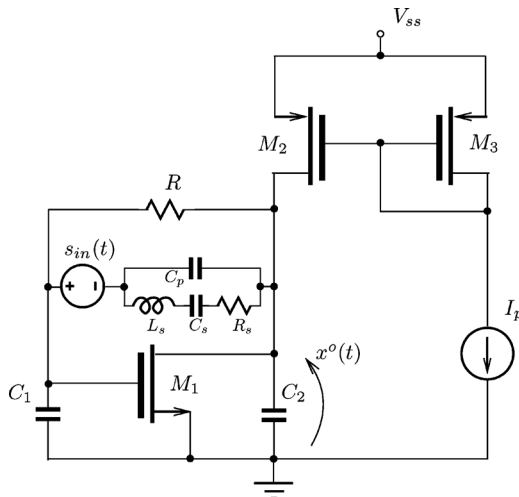
Fig. 6. Total jitter (solid line), PM-induced jitter (dashed line).

TABLE I
PARAMETERS OF THE PIERCE OSCILLATOR.

Parameter	Value
V_{ss}	1.5 V
I_p	30 μA
C_1	1.0 pF
C_2	1.0 pF
R_s	30 kΩ
C_s	3.6 fF
L_s	4.4 mH
C_p	100 fF
R	1 MΩ
$(W/L)_{2,3}$	200
$(W/L)_1$	2

TABLE II
FLOQUET EXPONENTS.

λ_2	$-2.51 \cdot 10^5$
λ_3	$-2.09 \cdot 10^6$
λ_4	$-2.30 \cdot 10^8$
λ_5	$-1.26 \cdot 10^9$

Fig. 7. Pierce crystal oscillator: R_s, C_s, L_s and C_p are the parameters of the crystal model. An interference signal is injected by the voltage source $s_{in}(t)$.

the time-domain simulator Simulation-LABoratory (S-LAB) [19], [20] and verified with SpectreRF.
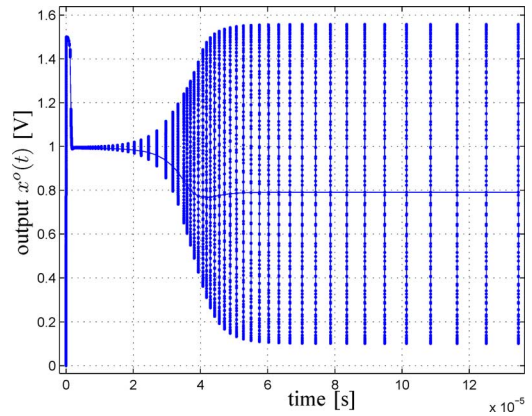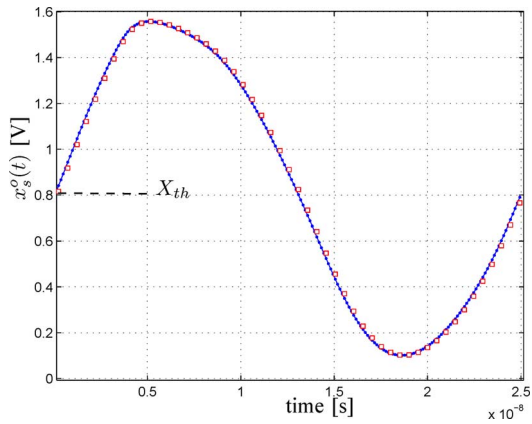

Fig. 8. Simulation results from envelope following.

Fig. 9. Ideal steady-state response $x_s^o(t)$: obtained with envelope (solid line), obtained with SpectreRF (square).
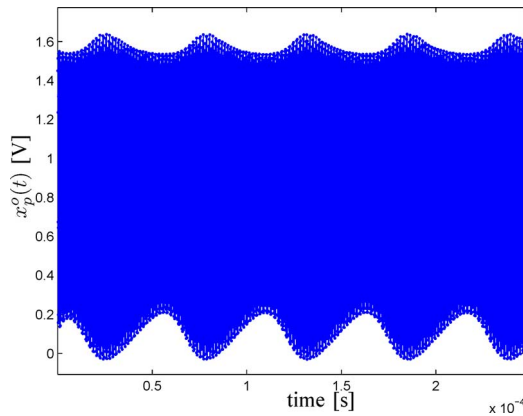
With the envelope-following algorithm [19], which is shortly reviewed in Appendix B, we simulate the time response of the free-running oscillator till the periodic steady state (PSS) is reached. We select the voltage across capacitor C_2 as the output variable the envelope of which is shown in Fig. 8.

Fig. 9 reports the (ideal) steady-state oscillatory response $x_s^o(t)$ over one cycle and compares it with that from SpectreRF simulation. The two waveforms match very well. The oscillating angular frequency is $\omega_0 = 252.007 \cdot 10^6$ rad/s and the period is $T_0 = 24.932$ ns.

Next, using the computational method described in Appendix A, we calculate the Floquet exponents/eigenfunctions along the stable orbit. Table II reports the Floquet exponents. From this table, we see that Floquet exponents are purely real and that $|\lambda_2| \ll |\lambda_{3,4,5}|$ dominates the amplitude response.

From the computed output-related elements of the first two right Floquet eigenvectors $u_1^o(t)$ and $u_2^o(t)$, we derive that for the threshold value $X_{th} = 0.8$ V, the ratio $R = u_2^o(0)/u_1^o(0) \approx 1$.

As an interfering signal, we consider the voltage source $s_{in}(t)$ inserted in series with the crystal quartz, as shown in Fig. 7, which represents a typical example of EMI [3]. The interfering signal is of the type (33) with amplitude $A_{in} = 100$ mV and varying frequency ω_{in}. Fig. 10 shows the first two projecting functions $\Gamma_1(t)$ and $\Gamma_2(t)$ associated with this interference:
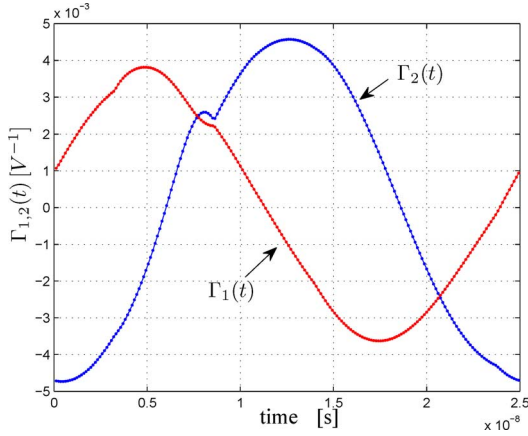
Fig. 10. Waveforms of $\Gamma_1(t)$ and $\Gamma_2(t)$ associated with interference $s_{in}(t)$.

Fig. 12. Perturbed response $x_p^o(t)$ over one working cycle: proposed macro-model (solid line), SpectreRF (square). The ideal response $x_s^o(t)$ (dashed line).

Fig. 11. Perturbed response $x_p^o(t)$ for $\omega_{in} = \omega_0 \times (1 - 5 \cdot 10^{-4})$.

Fig. 13. Deterministic jitter versus interference frequency.

both waveforms are dominated by the first harmonic component. Based on the theory developed in Section IV, we conclude that the interfering signal will induce significant jitter effects when its frequency ω_{in} is close to the fundamental frequency, i.e., $m = 1$ in (34). For the interference amplitude $A_{in} = 100$ mV, the lock range should be $B \approx 2 \cdot 10^{-4} \times \omega_0$. After that we sweep the value of the interference frequency ω_{in} in a frequency interval centered at ω_0. At each frequency point, we simulate the macromodel given by (19) and (28). In fact, ODE (28) only needs to be integrated for $k = 2, 3$ since $\tilde{y}_3(t)$ is about two orders of magnitude smaller than $\tilde{y}_2(t)$ and thus it can be neglected. Each simulation costs less than one second and allows us to efficiently derive the associated perturbed response $x_p^o(t) = x_s(t + \alpha(t)) + \Delta x^o(t + \alpha(t))$. Fig. 11 shows the perturbed response simulated with the compact macromodel for $\omega_{in} = \omega_0 \times (1 - 5 \cdot 10^{-4})$. This interference frequency falls outside the lock range and corresponds to a strong pulling scenario. Fig. 12 reports the perturbed responses over a cycle around $t = 0.14$ ms, which are computed by using our proposed macromodel and by detailed transistor-level simulation in SpectreRF, respectively. The two curves match excellently and exhibit a significant amplitude modulation effect.

It is worth noting that under the injection pulling regime the oscillator response is not periodic and its detailed simulation with SpectreRF aimed at finding the distribution of the perturbed period values is very time consuming. In fact, a great
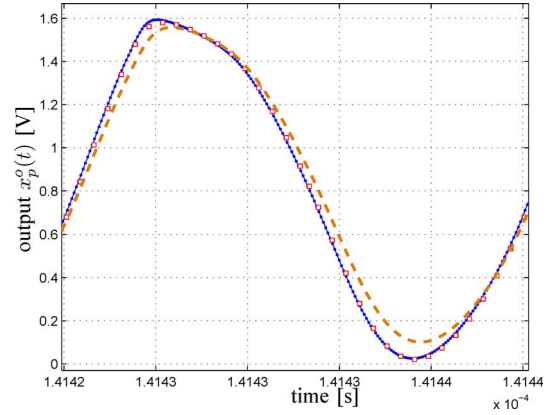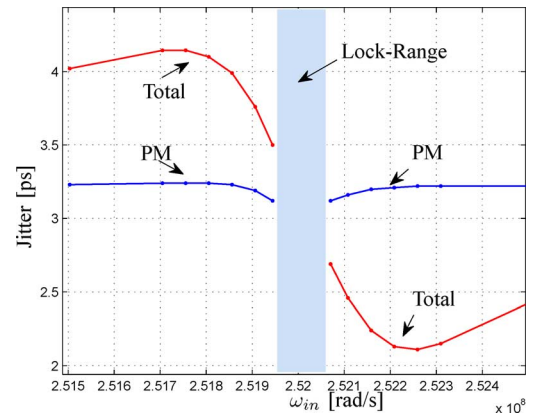
number of cycles have to be simulated and, in each cycle, a tiny time step is required to accurately calculate the threshold crossing time point. For this reason, SpectreRF simulations were employed only for the purpose of verification for a few values of ω_{in}.

For each perturbed response $x_p^o(t)$ simulated with our compact macromodel, we calculate a sequence of threshold crossing time points t_k and then compute the resulting timing jitter. Fig. 13 shows the computed total timing jitter and its component due to the PM effect only. The following observations are in order. As long as ω_{in} falls within the lock range, the deterministic timing jitter is zero. Outside the lock range, the PM-induced jitter is almost constant and does not depend on ω_{in}. For the parameters $T_0 = 24.932$ ns, $\Gamma_1^1 = 3.65 \cdot 10^{-3}$ V^{-1} and interference amplitude $A_{in} = 100$ mV, the analytical expression (46) yields $\sigma_T^{PM} = 3.21$ ps which matches excellently with the PM-induced jitter shown in Fig. 12. Besides, the dependence of the total jitter on the interference frequency fully confirms the theoretical explanation of the AM and PM effects interaction provided in Section IV: the total jitter has maximum/minimum values for $\omega_{in} \approx \omega_0 \mp |\lambda_2|$.

The impact of AM to the total jitter depends on ω_{in} in an asymmetric way. To further explore this point, Fig. 14 reports the histogram distribution of period values T_k for the two interference frequency values: (a) $\omega_{in} = \omega_0 \times (1 + 5 \cdot 10^{-4})$ and (b) $\omega_{in} = \omega_0 \times (1 - 5 \cdot 10^{-4})$, respectively. In Case (a) with
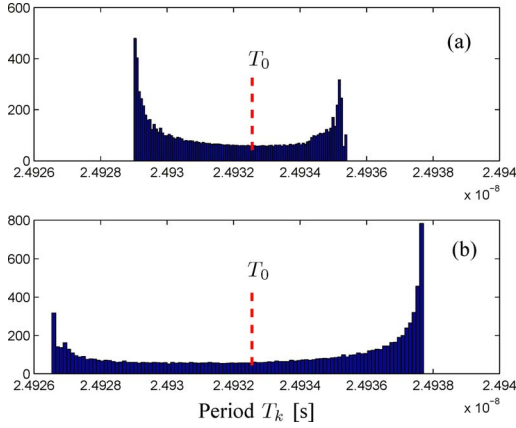
Fig. 14.   Distribution of perturbed period T_k in the cases (a) and (b).

$\omega_{in} > \omega_0$, the AM-induced period fluctuations tend to partly compensate the PM-induced ones. In Case (b) the AM-induced fluctuations add to the PM-induced ones, resulting in a wider period distribution and thus greater timing jitter.

VI. CONCLUSION

In this paper, the mechanism underlying deterministic timing jitter in crystal oscillators has been investigated. A variational compact macromodel has been proposed, which is able to include both phase and amplitude modulation effects. Starting from this macromodel, a closed-form expression for the timing jitter has been developed in the case of harmonic interferences. We have explored how the timing jitter depends on the frequency of the injected interference. We have also described how the parameters in our macromodel, i.e., the dominant Floquet exponents/eigenvectors, can be computed in a time domain simulator. We have further shown how the macromodel can be employed for numerically efficient behavioral simulations. Our proposed analysis methodology has been tested by a Pierce crystal oscillator.

APPENDIX A
FLOQUET THEORY OF LINEAR TIME-PERIODIC ODEs

The small perturbation $\delta\mathbf{x}(t)$ to the original PSS solution $\mathbf{x}_s(t)$ of the nonlinear autonomous ODE (1) can be studied by linearizing the ODE around the PSS solution and then applying Floquet theory. Linearization yields the following linear time-periodic ODE $x_s(t)$

$$\delta\dot{\mathbf{x}}(t) = \mathrm{Df}(\mathbf{x}_s(t)) \cdot \delta\mathbf{x}(t). \tag{58}$$

This linearized system admits N independent solutions

$$\exp(\lambda_k t)\mathbf{u}_k(t), \tag{59}$$

where the T_0-periodic vector $\mathbf{u}_k(t)$ is the kth right-side Floquet eigenvector and λ_k the corresponding Floquet exponent.

Similarly, the adjoint differential equation

$$(\delta\dot{\mathbf{x}}(t))^T = -(\delta\mathbf{x}(t))^T \cdot \mathrm{Df}(\mathbf{x}_s(t)) \tag{60}$$

admits the set of N independent solutions

$$\exp(-\lambda_k t)\mathbf{v}_k^T(t), \tag{61}$$

where vector $\mathbf{v}_k(t)$ is the left-side Floquet eigenvector. By inserting (61) into (60), we find

$$\mathbf{v}_k^T(t) \cdot \mathrm{Df}(\mathbf{x}_s(t)) = \lambda_k \mathbf{v}_k^T(t) - \dot{\mathbf{v}}_k^T(t). \tag{62}$$

Floquet eigenvectors satisfy biorthogonality condition

$$\mathbf{v}_k^T(t) \cdot \mathbf{u}_j(t) = \delta_{kj}, \tag{63}$$

in addition, we can choose

$$\mathbf{u}_1(t) = \dot{\mathbf{x}}_s(t). \tag{64}$$

For a stable limit cycle, the first Floquet exponent is $\lambda_1 = 0$ while the other exponents λ_k, with $k > 1$ have negative real parts.

APPENDIX B
COMPUTATIONAL ASPECTS

The numerical computation of Floquet exponents/eigenvectors relies on a two-step procedure. First, the PSS solution of a free-running crystal oscillator is determined. Next, the linear time-varying systems (58) and (60) are formed and solved in time. These steps are reviewed below.

Calculating the Steady-State Response $x_s(t)$ of Crystal Oscillators: Several periodic steady-state simulation techniques have been presented in the literature [22]. From a simulation point of view, crystal oscillators have high quality factors and tend to exhibit very long transient responses before reaching the steady-state regime. This can significantly degrade the numerical efficiency and robustness of PSS simulators. To overcome the limitation, Envelope-Following Method (EFM) is applied in our implementation [19], [22].

Floquet Parameters Computation: Once that the periodic steady-state solution has been computed over one period $(t_0, t_0 + T_0)$, the linear time-varying system (58) can be formed. The period is discretized at $M + 1$ consecutive time points $t_0, t_1, \dots, t_M$ with $t_M = t_0 + T_0$ and where $h_n = t_{n+1} - t_n$ is the local time step. When numerically integrated in time, the variational system (58) at time t_{n+1} is discretized, for instance, by adopting Backward Euler formula

$$\delta\mathbf{x}(t_{n+1}) - \delta\mathbf{x}(t_n) - h_n\mathbf{G}(t_{n+1})\delta\mathbf{x}(t_{n+1}) = 0, \tag{65}$$

where $\mathbf{G}(t_n) = \partial \mathbf{f}(\mathbf{x})/\partial \mathbf{x}|_{\mathbf{x}=\mathbf{x}_s(t_n)}$, leading to

$$(\mathbf{1}_N - h_n \mathbf{G}(t_{n+1}))\, \delta \mathbf{x}(t_{n+1}) = \delta \mathbf{x}(t_n). \tag{66}$$

The state transition matrix from t_n to t_{n+1} is obtained as

$$\mathbf{\Psi}_{n+1,n} = \frac{\partial \mathbf{x}(t_{n+1})}{\partial \mathbf{x}(t_n)} = (\mathbf{1}_N - h_n \mathbf{G}(t_{n+1}))^{-1}. \tag{67}$$

Hence the transition matrix over the whole period, i.e., the monodromy matrix, can be computed by the following matrix-by-matrix products

$$\mathbf{\Psi}_{M,0} = \frac{\partial \mathbf{x}(t_M)}{\partial \mathbf{x}(t_0)} = \mathbf{\Psi}_{M,M-1} \cdot \mathbf{\Psi}_{M-1,M-2} \dots \mathbf{\Psi}_{1,0}. \tag{68}$$

The monodromy matrix is related to Floquet eigenvalue/eigenvector through the following expansion

$$\mathbf{\Psi}_{M,0} = \sum_{k=1}^{N} \exp(\lambda_k T_0)\mathbf{u}_k(t_0)\mathbf{v}_k(t_0)^T, \tag{69}$$

thus from an eigenvalue and eigenvector expansion of $\mathbf{\Psi}_{M,0}$ matrix and its transpose, we can get λ_k and the eigenvectors $\mathbf{u}_k(t_0)$ and $\mathbf{v}_k(t_0)$ at the initial point t_0. The waveforms of $\mathbf{u}_k(t)$ and $\mathbf{v}_k(t)$ over the whole period are then recovered by integrating (58) forward and (60) backward, respectively. This results in the following recursive computations

$$\mathbf{u}_k(t_{n+1}) = \exp(-\lambda_k\, h_n)\mathbf{\Psi}_{n+1,n}\mathbf{u}_k(t_n) \tag{70}$$

and

$$\mathbf{v}_k^T(t_n) = \exp(-\lambda_k\, h_n)\mathbf{v}_k^T(t_{n+1})\mathbf{\Psi}_{n+1,n}, \tag{71}$$

from which we can get the results of $u_k(t)$ and $v_k(t)$ at a set of time points in the whole period.

References

[1] U. L. Rohde, A. K. Poddar, and G. Boeck, *The Design of Modern Microwave Oscillators for Wireless Applications: Theory and Optimization.* New York: Wiley, 2005.

[2] U. L. Rohde, A. K. Poddar, and R. Lakhe, "Electromagnetic interference and start-up dynamics in high-frequency crystal oscillator circuits," *Microwave Rev.*, no. 7, pp. 23–33, Jul. 2010.

[3] J. J. Laurin, S. G. Zaky, and K. G. Balmain, "EMI-induced failures in crystal oscillators," *IEEE Trans. Electromagn. Compat.*, vol. 33, no. 4, pp. 334–342, Nov. 1991.

[4] P. Wambacq, G. Vandersteen, J. Phillips, J. Roychowdhury, W. Eberle, B. Yang, D. Long, and A. Demir, "CAD for RF circuits," in *Proc. DATE*, Munich, Germany, 2001, pp. 520–529.

[5] L. Zhu and C. E. Christoffersen, "Transient and steady-state analysis of nonlinear RF and microwave circuits," *EURASIP J. Wireless Commun. Network.*, vol. 2006, pp. 1–11, 2006.

[6] F. X. Kaertner, "Analysis of white and $f^{-\alpha}$ noise in oscillators," *Int. J. Circuit Theory Applicat.*, vol. 18, no. 5, pp. 485–519, Sep. 1990.

[7] P. Vanassche, G. Gielen, and W. Sansen, "On the difference between two widely publicized methods for analyzing oscillator phase behavior," in *Proc. ICCAD*, Nov. 2002, pp. 229–233.

[8] A. Demir, A. Mehrotra, and J. Roychowdhury, "Phase noise in oscillators: A unifying theory and numerical methods for characterisation," *IEEE Trans. Circuits Syst.–I:Reg. Papers*, vol. 47, no. 5, pp. 655–674, May 2000.

[9] T. Lee and A. Hajimiri, "Oscillator phase noise: A tutorial," *IEEE J. Solid-State Circuits*, vol. 35, no. 3, pp. 326–336, Mar. 2000.

[10] D. Harutyunyan, J. Rommes, J. ter Maten, and W. Schilders, "Simulation of mutually coupled oscillators using nonlinear phase macromodels, "Applications"," *IEEE Trans. Comput.-Aided-Design Integrated Circuits Syst.*, vol. 28, no. 10, pp. 1456–1466, Oct. 2009.

[11] P. Maffezzoni, "Synchronization analysis of two weakly coupled oscillators through a PPV macromodel," *IEEE Trans. Circuits Syst.–I:Reg. Papers*, vol. 57, no. 3, pp. 654–663, Mar. 2010.

[12] M. M. Gourary, S. G. Rusakov, S. L. Ulyanov, M. M. Zharov, and B. J. Mulvaney, J. Roos and L. R. J. Costa, Eds., "Evaluation of oscillator phase transfer functions," in *Proc. SCEE*, 2008, vol. 14, Mathematics in Industry, pp. 183–190.

[13] M. Bonnin, F. Corinto, and M. Gilli, "Phase space decomposition for phase noise and synchronization analysis of planar nonlinear oscillators," *IEEE Trans. Circuits Syst.–II:Brief Papers*, vol. 59, no. 10, pp. 638–642, Oct. 2012.

[14] M. Bonnin and F. Corinto, "Phase noise and noise induced frequency shift in stochastic nonlinear oscillators," *IEEE Trans. Circuits Syst.–I:Reg. Papers*, vol. 6, no. 8, pp. 2104–2115, Aug. 2013.

[15] X. Lai and J. Roychowdhury, "Capturing oscillator injection locking via nonlinear phase-domain macromodels," *IEEE Trans. Microwave Theory Tech.*, vol. 52, no. 9, pp. 2251–2261, Sep. 2004.

[16] X. Lai and J. Roychowdhury, "Automated oscillator macromodelling techniques for capturing amplitude variations and injection locking," in *Proc. IEEE Int. Conf. Comput.-Aided Design*, Nov. 2004.

[17] R. Adler, "A Study of locking phenomena in oscillators," in *Proc. IRE Waves Electrons*, Jun. 1946, vol. 34, pp. 351–357.

[18] M. Farkas, *Periodic Motions*. : Springer-Verlag, 1994.

[19] P. Maffezzoni, "A versatile time-domain approach to simulate oscillators in RF circuits," *IEEE Trans. Circuits Syst.–I:Reg. Papers*, vol. 56, no. 3, pp. 594–603, Mar. 2009.

[20] P. Maffezzoni, L. Codecasa, and D. D'Amore, "Time-domain simulation of nonlinear circuits through implicit Runge-Kutta methods," *IEEE Trans. Circuits Syst.–I:Reg. Papers*, vol. 54, pp. 391–400, Feb. 2007.

[21] L. Petzold, "An efficient numerical method for highly oscillatory ordinary differential equations," *SIAM J. Numer. Anal.*, vol. 18, no. 3, Jun. 1981.

[22] K. Kundert, J. White, and A. Sangiovanni-Vincentelli, *Steady-State Methods for Simulating Analog and Microwave Circuits*. New York: Springer, 1990.

Paolo Maffezzoni (M'08) received the Laurea degree (summa cum laude) in electrical engineering from the Politecnico di Milano, Italy, in 1991 and the Ph.D. degree in electronic instrumentation from the Università di Brescia, Brescia, Italy, in 1996.

In 1998, he joined the Politecnico di Milano, as an Assistant Professor, where he has been an Associate Professor of Electrical Engineering since 2004. His research interests are in the area of modeling, analysis and simulation of nonlinear circuits and systems with particular emphasis on analog and RF communication electronics. On this subject he has published about 120 papers in international journals and refereed conferences.
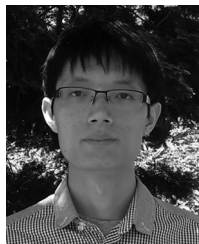
Zheng Zhang (S'09) received the B.Eng. degree from Huazhong University of Science and Technology, China, in 2008, and M.Phil. degree from the University of Hong Kong, Hong Kong, in 2010. He is a Ph.D student in electrical engineering at the Massachusetts Institute of Technology (MIT), Cambridge, MA, USA.

His research interests include uncertainty quantification (UQ), computer-aided design (CAD) of integrated circuits and microelectromechanical systems (MEMS), and model order reduction. In 2009, He was a Visiting Scholar with the University of California, San Diego, La Jolla, CA USA. In 2011, he collaborated with Coventor Inc., working on CAD tools for MEMS design. In 2013, he was a Visiting Scholar at Brown University, Providence, RI.

Mr. Zhang was the recipient of the Li Ka Shing Prize (university best M.Phil./Ph.D. thesis award) from the University of Hong Kong, in 2011, and the Mathworks Fellowship from MIT, in 2010.

Luca Daniel (S'98-M'03) received the Laurea degree (summa cum laude) in electronic engineering from the Università di Padova, Padua, Italy, in 1996, and the Ph.D. degree in electrical engineering from the University of California, Berkeley, CA, USA, in 2003.

He is an Associate Professor in the Electrical Engineering and Computer Science Department, Massachusetts Institute of Technology, Cambridge, MA, USA. His current research interests include accelerated integral equation solvers and parameterized stable compact dynamical modeling of linear and nonlinear dynamical systems with applications in mixed-signal/RF/mm-wave circuits, power electronics, MEMs, and the human cardiovascular system.

Dr. Daniel was a recipient of the 1999 IEEE Transactions on Power Electronics Best Paper Award, the 2003 ACM Outstanding Ph.D. Dissertation Award in Electronic Design Automation, five Best Paper Awards in international conferences, the 2009 IBM Corporation Faculty Award, and 2010 Early Career Award from the IEEE Council on Electronic Design Automation.